Environmental Stress-Based Reliability Assessment of Power Distribution Systems: An Integrated Multi-Physics Methodology

Roberto Ciavarella * and Maria Valenti

Posted Date: 30 March 2026

doi: 10.20944/preprints202603.2315.v1

Keywords: reliability assessment; power distribution; OpenDSS; Norris-Landzberg; environmental stress; asset management; Weibull distribution

 doi:10.20944/preprints202603.2315.v1

Article

Environmental Stress-Based Reliability Assessment of Power Distribution Systems: An Integrated Multi-Physics Methodology

Roberto Ciavarella * and Maria Valenti

ENEA-Italian National Agency for Energies, New Technologies and Sustainable Economic Development, 00196 Rome, Italy

* Correspondence: roberto.ciavarella@enea.it

Abstract

Traditional reliability models for distribution grids often rely on static historical averages, overestimating the operational lifespan of power system assets by neglecting the dynamic interplay between electrical loading and microclimatic stressors. This paper addresses these limitations by introducing an innovative multi-physics methodology that shifts the analytical paradigm toward a Physics-of-Failure (PoF) approach. This methodology is operationalized through a novel simulation framework and a modular Python-based tool, integrating OpenDSS and Pandapower to perform high-fidelity reliability assessments. By calculating instantaneous failure rates and Mean Time Between Failures (MTBF) as functions of real-time environmental forcing—specifically temperature and humidity-induced stresses—the proposed system captures degradation dynamics that remain invisible to conventional models. The framework's capabilities are demonstrated through a simulation on a rural distribution grid, which explicitly includes auxiliary digitalization components, such as Remote Terminal Units (RTUs), that are frequently overlooked in standard benchmarks. The results reveal that environmental forcing triggers a severe contraction in the MTBF of critical active assets, proving that asset seniority alone is an insufficient proxy for grid vulnerability. Furthermore, the integration of an advanced Reliability Dashboard enables Distribution System Operators (DSOs) to conduct sophisticated "What-If" analyses and quantify Expected Risk Costs (ERC) prior to physical deployment. Ultimately, this research provides a robust, innovation-driven decision-support system for the cost-effective hardening of smart grids, bridging the gap between theoretical power flow analysis and proactive, climate-resilient asset management.

Keywords: reliability assessment; power distribution; OpenDSS; Norris-Landzberg; environmental stress; asset management; Weibull distribution

1. Introduction

Ensuring the reliability of power distribution systems has long been a central concern for utilities and system operators, as continuity of service directly influences infrastructure resilience, public welfare, and overall economic performance. Failures of key assets such as power transformers or distribution lines can trigger cascading outages, leading not only to substantial financial losses for Distribution System Operators (DSOs) but also to broader societal impacts, including service disruptions, reduced grid stability, and increased vulnerability to subsequent disturbances [1]. Traditional reliability assessment methodologies typically rely on historical failure statistics, simplified static component models, and Monte Carlo–based simulations to derive indices such as SAIDI, SAIFI, and ENS. These approaches largely assume stationary operating conditions and constant failure rates, drawing on averaged historical data and age-based component representations. However, such assumptions prevent them from capturing the increasing variability introduced by distributed energy resources (DERs) and the growing influence of extreme environmental stressors [2]. Although these methods still provide a baseline for long-term planning,

 doi:10.20944/preprints202603.2315.v1

they fail to adequately reflect localized stressors and are becoming increasingly insufficient under climate-driven risk conditions.

Recent research has advanced reliability modeling by incorporating distributed generation, ICT infrastructure, and operational dynamics. For example, Parol et al. [3] proposed detailed reliability models for medium voltage networks that integrate conventional and renewable energy sources alongside ICT components, demonstrating how system structure and automation schemes influence reliability outcomes. Similarly, Karngala et al. [4] introduced a bottom-up probabilistic reliability framework that captures heterogeneity in residential DER adoption, showing that differing customer-level PV and storage deployment scenarios can widen the distribution of reliability outcomes across users. In parallel, research on extreme weather impacts has expanded significantly, with Téllez et al. [5] presenting a weather-aware probabilistic framework that models extreme weather events as high-impact multipliers of component failure and repair uncertainty. Broader reviews and empirical studies [6–10] reinforce these findings, highlighting that extreme weather events—including heatwaves, windstorms, and freezing conditions—are now responsible for a substantial share of global outages. These trends underscore the need for methodologies that capture dynamic environmental stressors and account for the escalating risks posed to transmission and distribution assets.

Despite these advancements, two major limitations remain in the state of the art. First, most existing reliability models integrate weather effects only through coarse escalation factors or historical correlations, rather than explicit multi-physics representations of how environmental stressors affect component-level degradation. Second, although some probabilistic frameworks account for climate-driven variability, they often decouple environmental stress modeling from network-level reliability evaluation, limiting their ability to quantify propagation effects across the distribution system. To address these gaps, this work, a direct extension of our previous studies [11–13], proposes an integrated multi-physics, Python-based reliability assessment tool that embeds environmental stressors directly into component-level reliability models. The methodology incorporates thermal and environmental acceleration factors into failure rate estimation, enabling the representation of how events such as heatwaves alter aging mechanisms and operational margins of key distribution components. By transitioning from a component-level stress analysis to a comprehensive system-wide reliability evaluation, the proposed approach provides a more granular and accurate prediction of grid reliability.

A key innovation of this methodology is the explicit decoupling and subsequent integration of two distinct reliability layers: the Physical Infrastructure Layer and the Cyber-Control Layer. While the former is subject to failure rates dynamically scaled by environmental stressors, the latter accounts for the operational availability of Remote Terminal Units (RTUs) and communication links. This ability to virtualize the grid's control layer expands modeling capabilities beyond what is available in standard benchmark networks, such as CIGRE [14], which do not natively include automation or communication assets. In real-world systems, RTUs enable fault detection, isolation, service restoration, and continuous observability, playing a critical role in ensuring the reliable operation of modern smart grids. The proposed tool extends the benchmark's scope by simulating RTUs at critical nodes, enabling the representation of measurement acquisition, remote control capabilities, and communication-related uncertainty within the reliability evaluation. This aligns with research [3,15,16] confirming that the presence, density, and reliability of RTUs have a measurable impact on outage reduction and network resilience. Through this integrated pipeline, the approach bridges the disconnect between detailed physical stress modeling and holistic distribution network evaluation, providing a more realistic and actionable assessment of reliability under emerging climate conditions.

The paper is structured as follows: Section 2 introduces the methodology; Section 3 presents the case study and the simulation tests, and Section 4 discusses the results; Section 5 concludes the work and highlights future developments.

 doi:10.20944/preprints202603.2315.v1

2. Methodology

The proposed research follows a structured developmental pipeline, transitioning from theoretical formulation to computational implementation. The proposed methodology introduces a mathematical approach to shift from constant failure rates to dynamic, stressor-dependent functions by mapping thermal and environmental variables onto the hazard rate $\lambda(t)$. This redefinition allows for a realistic assessment of component aging and operational risk under varying climatic conditions, specifically by integrating ambient temperature as a primary driver of physical degradation. This conceptual backbone is operationalized through a modular framework designed to ingest heterogeneous data sources, including power grid topologies and climate datasets and then a modular Python-based tool has been developed to automate the execution of these high-fidelity reliability simulations. This tool integrates power flow engines like OpenDSS and Pandapower with the Physics-of-Failure (PoF) methodology, enabling the seamless translation of raw microclimatic data into actionable reliability metrics. By bridging the gap between the theoretical formulation and practical grid management, the tool provides a scalable environment where the vulnerability of each asset—from primary transformers to auxiliary digitalization components—can be quantified and visualized through an integrated risk dashboard. This section provides a detailed technical breakdown of this framework. Hereafter, a comprehensive breakdown of the framework's architecture is provided, with a primary focus on its core engine: the Multi-Physics Reliability Modeling. The implementation of the proposed methodology across diverse grid assets is then detailed, illustrating how specific environmental and operational degradation drivers are uniquely mapped onto the failure physics of each considered component typology.

2.1. Framework Architecture

The framework orchestrates the interaction between thermal degradation models and system-wide reliability indices, ensuring a scalable workflow applicable to different geographical regions or network configurations. This integrated approach is implemented in a dedicated Python-based software tool, which provides a computational environment for sensitivity analyses and stress-tests, computing standard reliability indices such as LOLE or EENS while accounting for climate-driven fluctuations.

The framework's architecture is orchestrated as a multi-layered computational pipeline, developed entirely in Python to ensure seamless interoperability between power systems engineering and climate science data. The methodology relies on a hybrid integration of two industry-leading libraries: OpenDSS [5] and Pandapower [9]. This strategic "dual-engine" approach is motivated by the specific requirements of multi-physics analysis:

- OpenDSS (via opendssdirect): Acts as the high-performance QSTS solver. It was selected for its superior ability to handle unbalanced distribution systems and its computational efficiency in processing 8,760 hourly steps. This engine is responsible for solving the physical state of the grid, producing the time-varying current and voltage profiles for every asset.
- Pandapower: Serves as the topological and data management layer. Its pandas-based structure allows for the flexible injection of external datasets (such as hourly ambient temperature or humidity) directly onto the network graph. It is used to post-process the electrical results and map them to the corresponding reliability models.

A core technical contribution of this work is the development of an automated conversion pipeline. Given that network models are often provided in proprietary or vendor-specific formats, the tool implements a topology-agnostic logic that translates .dss files into a Python-native environment. This process ensures:

- Fidelity of Electrical Parameters: Automated mapping of line impedances, transformer tap-changers, and DER (Distributed Energy Resources) configurations.
- Geographical Consistency (GIS): The pipeline preserves the XY coordinates of every node and branch. This spatial integrity is crucial for correlating each asset with localized climatic stressors,

 doi:10.20944/preprints202603.2315.v1

such as specific soil thermal resistivity for buried joints or localized wind exposure for overhead lines.

- Sub-Component Injection: The code explicitly identifies and isolates critical sub-elements—specifically cable joints and protection devices—which are often simplified in standard load-flow tools but are primary failure points in reliability studies.

The framework features an Integrated Reliability Dashboard. This visualization layer acts as the final stage of the computational pipeline, converting high-dimensional stochastic data into an actionable diagnostic interface. The dashboard is structured into four primary functional modules:

- Geospatial Network Health Mapping: The central component is a topological representation of the distribution grid where every asset is dynamically color-coded based on its estimated Mean Time Between Failure (MTBF). This allows for the immediate identification of critical hotspots—highlighted in red for high-risk segments—and optimal zones, preserving the GIS consistency of the original network model.
- Weighted System KPIs: A dedicated panel aggregates the electrical performance into standardized reliability indices, including SAIFI, SAIDI, and CAIDI. This section provides a macro-level assessment of the network's quality of service, distinguishing between the average MTBF of overhead lines and underground cables to identify the most vulnerable infrastructure types.
- Multi-Physics Stressor Correlation: The dashboard shows a dominant cause analysis alongside temporal climate profiles. A categorical distribution (pie chart) identifies the primary drivers of failure—such as wind-induced mechanical stress or thermal degradation—while a series of time-series plots track variables like Ambient Temperature, Solar Irradiation, Wind Speed, and Humidity over an annual horizon. This module allows researchers to correlate specific failure peaks with extreme weather events or seasonal environmental loads.

Localized Asset Vulnerability Ranking: The dashboard includes a tabular ranking of the "Top 10" critical assets based on their annual MTBF. This granular view identifies specific component types (e.g., inverters or converters) and their dominant failure modes, enabling a transition from system-wide statistics to targeted predictive maintenance strategies.

2.2. Software Architecture

The software architecture is organized into five main functional blocks that transform deterministic electrical simulations into stochastic reliability assessments.

The first block, **Network Ingestion block**, manages the parsing and mapping of grid topologies into a unified internal representation, utilizing pandapower for core network management and opendssdirect for high-fidelity simulations. This layer characterizes assets with high granularity, distinguishing between overhead lines and underground cables while identifying critical sub-components such as cable joints, circuit breakers, and Remote Terminal Units (RTUs).

Following ingestion, the **Quasi-Static Time-Series** (QSTS) **Simulation block** captures the dynamic interplay between renewable generation, demand, and thermal inertia. By employing a multi-algorithm strategy—including Newton-Raphson and FDBM—to ensure convergence across 8,760 hourly points, this block generates the loading profiles and voltage magnitudes that serve as the foundation for subsequent aging models.

The analytical core of the tool resides in the **Multi-Physics Reliability Mapping block**, which implements an advanced Norris-Landzberg and Arrhenius-based mapping through a specialized ReliabilityModel class. For each component, the tool calculates a time-dependent failure rate by integrating internal temperature rises derived from Joule losses and solar gain with stochastic modeling of environmental stressors, such as wind gusts via Weibull distributions, humidity-induced corrosion through Peck's model, and soil resistivity variations. This block explicitly accounts for asset-specific degradation, including localized hotspots in cable joints and mechanical fatigue in overhead conductors using the Coffin-Manson approach for thermal cycling and Aeolian vibration models for wind-induced stress.

 doi:10.20944/preprints202603.2315.v1

These granular failure rates are then processed by the **KPI Aggregation block**, which computes system-level indices including SAIFI (System Average Interruption Frequency Index), SAIDI (System Average Interruption Duration Index), and CAIDI (Median restoration time under stressed conditions). To ensure realism, the framework applies to a Mean Time To Repair (MTTR) matrix weighted by weather severity, where extreme conditions (wind or rain) introduce a calculated "weather delay" factor.

Finally, the **Economic Risk Analysis block** translates these technical indicators into a Decision Support System (DSS) for Distribution System Operators (DSOs) by calculating the Annualized Risk Cost ($R=\frac{CAPEX}{MTBF}$), enabling a comparative analysis between "Baseline" and "Climate-Stressed" scenarios. This allows for the prioritization of asset replacement and targeted OPEX allocation based on the quantified impact of global warming on the grid's structural integrity.

2.3. Multi-Physics Reliability Mapping block

This section details the dynamic reliability formulation and Physics-of-Failure (PoF) modeling within the Multi-Physics Reliability Mapping block (Section 2.3.1), followed by the specific characterization of grid components subjected to multi-physics stressors (Sections 2.3.2–2.3.5)

2.3.1. Dynamic Reliability Formulation and Physics-of-Failure Modeling

To bridge the gap between the computational framework and the assessment of grid reliability, this section defines the analytical engine, the ReliabilityModel class, used to transform environmental stressors into dynamic failure rates, transitioning from a statistical baseline to the specific physical characterization of each grid asset.

The reliability of individual components, accounting for climatic stressors, is calculated using Eq. (1). Specifically, for each component i at each simulation step t, the framework calculates an instantaneous failure rate $\lambda_i(t,\tau)$:

$$\lambda_i(t) = \lambda_{base,i}(t) \cdot \pi_{tech,i} \cdot \prod_k \pi_{k,i}\left(\mathbf{x}(t)\right) \qquad (1)$$

where $\lambda_{base,i}(t)$ represents the statistical aging (Eq. 2), and $\pi_{tech,i}$ is the technology-specific calibration factor , and $\pi_{k,i}$represents the k-th physical stress factor (e.g., temperature, voltage, wind speed, humidity) derived from the state vector $\mathbf{x}(\tau)$.

More in detail:

- The intrinsic wear-out $\boldsymbol{\lambda_{base,i}(t)}$ follows a two-parameter Weibull distribution [17] modeling the probability of failure as a function of the asset's age:

$$\lambda_{base}(t) = \frac{\beta}{\alpha}\left(\frac{t}{\alpha}\right)^{\beta-1} \qquad (2)$$

- The **Technology Factor (π_{tech})** is a fundamental calibration constant that accounts for the inherent complexity and vulnerability of the asset's internal architecture [18]:
  - $\pi_{tech,Passive/Structural\ Assets} = 1.00$

    This value is assigned to overhead lines, underground cables, and transformers. These are high-inertia components whose degradation is primarily driven by long-term material fatigue or insulation breakdown.
  - $\pi_{tech,Cable\ Joints} = 1.20$

    This value is driven by risks related to the manual assembly of the cable joints.
  - $\pi_{tech,\text{Active Power Electronics}} = 1.25$

 doi:10.20944/preprints202603.2315.v1

This value is related to PV Inverters and RTUs. It accounts for the sensitivity of high-frequency switching semiconductors and control circuitry to thermal cycles and transients [19].

- $\pi_{tech,\text{Electrochemical Systems}} = 2.00$

  Specifically for BESS, reflecting the coupled complexity of chemical cell degradation (e.g., SEI layer growth) and the active power electronics of the Battery Management System (BMS) [20].

Then, to quantify the network's State of Health (SoH) at each simulation step t, the framework evaluates an instantaneous Mean Time Between Failures (MTBF), defined as the reciprocal of the total hazard rate:

$$MTBF(t)_i = \frac{1}{\lambda_i(t)} \quad (3)$$

This metric provides a high-fidelity proxy for the asset's vulnerability to current environmental and operational forcing. By evaluating $\frac{1}{\lambda(t)}$, the model captures the 'reliability margin' remaining under specific stress conditions. A sharp contraction in the during extreme weather events directly reflects the accelerated aging and the temporary increase in failure probability, serving as a dynamic trigger for predictive maintenance and grid resilience assessment.

For an 8,760-hour annual simulation, the Multi-Physics Reliability Mapping block requires two primary time-series datasets for each component:

- Electrical Profiles: These consist of normalized hourly load shapes (expressed in per-unit of the peak demand) and solar irradiance profiles (W/m²). These profiles are assigned to specific buses and photovoltaic (PV) installations within the network.
- Climatic Profiles: To account for environmental uncertainty, the tool processes stochastic hourly series for ambient temperature (T_{amb} − °C), wind speed (v_w − m/s), and relative humidity (H_{rel} − %). These variables are not treated as static averages but as dynamic stressors that, depending on the specific scenario, fluctuate or vary according to predefined laws (e.g., a Weibull distribution has been used to model random wind gusts).

All additional parameters required for running the block (e.g., a, β, π_{tech}, etc.) are preloaded within the software models.

2.3.2. Transformer Thermal and Degradation Modeling

The diagnostic model for the 'Transformer' category is grounded in the thermal equilibrium equations defined by the IEEE C57.91-2011 and IEC 60076-7 standards. The model integrates a deterministic thermal core with non-linear stochastic penalties for extreme environmental stressors.

The reliability of a power transformer is not a static parameter but a dynamic function of its thermal history and environmental context. The following sections detail the sequential derivation of the failure rate λ.

The Thermal Engine: Top-Oil Temperature (Toil)

The process begins with the estimation of the Top-Oil Temperature (T_{oil}), which represents the thermal stressor acting upon the solid and liquid insulation. According to the IEEE C57.91-2011 standard, T_{oil} is determined by the balance between the heat generated by the load and the ambient cooling capacity:

$$T_{oil,i} = T_{amb,i} + (\Delta T_{rated} \cdot L_i^n) \quad (4)$$

 doi:10.20944/preprints202603.2315.v1

In this model, L_i is the per-unit loading profile, ΔT_{rated}=40 K is the full-load temperature rise, and n=1.8 is the exponent for ONAN (Oil Natural, Air Natural) cooling configuration. This vector T_{oil} is critical because its extreme values and its range define the subsequent degradation factors.

Thermo-Mechanical Cycling

The Toil vector is processed to extract two fundamental parameters: the annual peak temperature (T_max=max(T_{oil})) and the thermal excursion range ($\Delta T_{cycling}$=T_{max}−T_{min}). These values serve as inputs for the Norris-Landzberg equation [21], which models the cumulative damage to the cellulose paper and the mechanical clamping of the windings:

$$\pi_{si} = \left(\frac{12 \cdot \eta_{cy}}{8760}\right) \cdot \left(\frac{\Delta T_{cycling}}{T_{ref}}\right)^{m} \cdot \exp\left[B\left(\frac{1}{T_0} - \frac{1}{T_{max} + 273.15}\right)\right] \qquad (5)$$

Here, the T_{oil} dynamics are converted into a structural integrity factor π_{si}. The term $\Delta T_{cycling}$ represents the magnitude of mechanical strain due to differential thermal expansion, while the Arrhenius exponential (with B=1414 and T_0=323.15 K) accounts for the accelerated chemical depolymerization of the paper insulation at the peaks of Toil.
The parameter η_{cy} represents the annual frequency of thermal cycles (heating and cooling events) extracted from the operating temperature profile via cycle-counting algorithms, accounting for the cumulative mechanical fatigue induced by load fluctuations and intermittent renewable generation.

Multi-Stress Integration and Failure Rate (λ)

The final stage of the model integrates the thermal-mechanical factor (π_{si}) with dielectric and environmental stressors to modulate a Weibull failure rate. The voltage stress π_V (even small increases in operating voltage (>2%) can lead to an exponential increase in partial discharge activity, significantly accelerating the aging of the oil-paper insulation) and the climatic impact $\pi_{extreme}$ (aggregating heatwaves and humidity) are combined with π_{si} to adjust the aging kinetics:

$$\lambda_{clima}(t) = \frac{\beta}{\alpha} \cdot \left(\frac{t}{\alpha}\right)^{\beta-1} \cdot \pi_{total} \qquad (6)$$

where the total stress aggregator π_{total} is defined as:

$$\pi_{total} = \pi_{tech} \cdot \pi_v \cdot (\pi_{si} + \pi_e + \pi_q + \pi_{extreme}) \quad (7)$$

The total stress factor π_{total} is a dimensionless multiplier that scales the baseline failure rate. It represents the synergy between intrinsic asset quality and extrinsic operating conditions.
The intrinsic quality factors (π_{tech}, π_q, π_e) represent:

- π_{tech} **(Technical Index):** A baseline performance coefficient (set to 0.85 in this model). It accounts for the specific transformer technology and its efficiency. A value < 1 suggests a higher-than-average initial health state.
- π_q **(Quality Factor):** Represents the manufacturing quality and the reliability of the supply chain.
- π_e **(External/Installation Factor):** Accounts for the quality of the installation and the specific environment of the substation (e.g., presence of saline mist, pollution).

 doi:10.20944/preprints202603.2315.v1

- $\pi_{extreme}$: A balanced sum of stressors that are usually external to the standard thermal model:

$$\pi_{extreme} = \mathrm{I}_{heat} + I_{humidity} \quad (8)$$

$\mathrm{I}_{heat} = 0.15 \cdot (\frac{T\_max}{48})^2$: Triggers above 48°C, accounting for the failure of the cooling system to maintain safe margins.

$I_{humidity}$: Set to 0.005 if H(humidity) > 95% , representing the risk of moisture ingress in the insulation or the degradation of the oil's dielectric breakdown voltage.

2.3.3. Transmission Lines and Underground Cables Modeling

The reliability of transmission assets is a dynamic function of the conductor's operating temperature (T_{op}), which affects both mechanical integrity in overhead lines and dielectric stability in buried cable joints. This section details the physics-based modeling of these assets and the subsequent failure rate derivation.

Thermal Equilibrium of Overhead Lines (OHL)

For aerial conductors, the model adopts the steady-state heat balance equations defined in IEEE Std 738. The operating temperature (T_{op}) is determined by the equilibrium between internal Joule heating, solar radiative gain, and convective cooling:

$$T_{op,i} = T_{amb,i} + (Q_{solar,i} \cdot \gamma)(L_i^2 \cdot \Phi \cdot \psi_{wind}) \quad (9)$$

Where:

- $T_{amb,i}$ [°C]: Instantaneous ambient air temperature.
- $Q_{solar,i}$ [W/m2]: Global solar radiation.
- γ: Solar absorption coefficient (dimensionless, range 0.5–0.9), representing the radiative heat gain based on the conductor's surface emissivity and oxidation state.
- L_i [p.u.]: Per-unit loading of the line (Iactual/Irated).
- Φ: Thermal Proportionality Constant. In this model, Φ is defined as the maximum Joule-induced temperature rise at rated load under stagnant air conditions. For standard ACSR (Aluminum Conductor Steel Reinforced) lines, Φ is set to 25.0 K
- ψ_{wind}: Convective cooling factor, modeled as $1/(1+0.1 \cdot V_{w,i})$, where $V_{w,i}$ is the cross-flow wind velocity [m/s].

A critical aspect of OHL reliability is the Thermal Sagging phenomenon. When T_{op} exceeds the safety limit of 75°C, the conductor enters a regime of irreversible mechanical elongation due to the annealing of the aluminum strands. This elongation increases the vertical sag of the span, violating the minimum ground clearance distances.

In this model, the risk is quantified by a discrete impact factor:

$$\mathrm{I}_{heat} = 0.2 \; if \; T_{op} > 75\,°C \quad (10)$$

This factor accounts for the surge in probability of phase-to-ground flashover and the permanent loss of tensile strength in the conductor.

The climatic impact for OHL is specifically weighted to reflect aerial vulnerabilities:

$$\pi_{extreme} = \mathrm{I}_{heat} + I_{wind} + I_{humidity} \quad (11)$$

 doi:10.20944/preprints202603.2315.v1

For overhead lines, the model incorporates two specific stochastic penalties to account for mechanical instability and insulation degradation:

- Wind-Induced Mechanical Stress (I_{wind})
- Humidity and Pollution Flashover $(I_{humidity})$

Wind speeds exceeding **20.0 m/s** (approx. 72 km/h) trigger a quadratic penalty factor to model structural risks such as **Galloping** and **Aeolian Vibrations**:

$$I_{wind} = 0.3 \cdot (\frac{V_{max}}{20})^2 \quad if \quad V_{max} > 20\ m/s \qquad (12)$$

High winds induce low-frequency, high-amplitude oscillations (galloping). This phenomenon causes severe mechanical stress on cross-arms, insulators, and the conductor strands themselves at the suspension points. The use of a squared ratio reflects the physical law where wind pressure (and thus the kinetic energy transferred to the structure) increases with the square of the velocity.
The model applies a discrete penalty ($I_{humidity} = 0.15$) when the relative humidity remains consistently above 90%. High humidity levels, often associated with fog or heavy mist, promote the formation of a conductive moisture film on the surface of ceramic or composite insulators. If the insulators are contaminated (salt, dust, or industrial pollutants), this moisture layer facilitates leakage currents, significantly increasing the probability of a dry-band arcing or a complete phase-to-ground flashover.

Thermal and Reliability Model for Underground Cables (UGC)

In contrast to overhead lines, the reliability of underground cables is governed by the thermal interaction between the conductor and the surrounding soil. The model transitions from atmospheric convection to conduction-based heat dissipation, following the principles of the Neher-McGrath method for calculating the current-carrying capacity of cables.
The critical factor for underground heat dissipation is the soil's thermal resistivity (ρ_{soil}). While air cooling is relatively consistent, soil resistivity is highly sensitive to moisture content. The model adopts an exponential decay function to simulate how drought conditions (low humidity) inhibit thermal dissipation:

$$\rho_{soil} = 1.0 + 3.5 \cdot e^{-0.07 \cdot H} \qquad (13)$$

Where:

- H [%]: Local soil moisture/humidity proxy.
- ρ_{soil} [K·m/W]: Soil thermal resistivity. As humidity drops below 30%, ρ_{soil} increases sharply, leading to a "thermal runaway" risk where the soil dries out further due to the cable's own heat.

The operating temperature of the buried conductor is determined by its depth and the thermal resistance of the ground (R_{ground}), modeled as:

$$R_{ground} = \frac{\rho_{soil}}{2\pi} \cdot \ln(\frac{4 \cdot D}{d}) \qquad (14)$$

- **D[m]:** Burial depth (default 1.0m).
- **d[m]:** Cable diameter (constant factor 0.05m).

 doi:10.20944/preprints202603.2315.v1

The resulting temperature T_{op} integrates the effective ground temperature (T_{ground}) and the Joule heating rise:

$$T_{op} = T_{ground} + (L^2 \cdot 0.012 \cdot R_{ground} \cdot 25) \quad (15)$$

Where:

- T_{ground} [°C]: The lagged soil temperature.
- L [p.u.]: Per-unit loading of the line (Iactual/Irated).
- R_{ground}: Thermal resistance of the surrounding earth.
- 25.0 [K]: The Thermal Proportionality Constant. This represents the maximum Joule-induced temperature rise at rated load (L=1.0) under standard soil conditions. It acts as the "thermal engine" of the cable, which is then scaled by the loading square and environmental resistance.
- 0.012: A normalization factor to align the I^2R gradient with standard XLPE/EPR cable specifications.

Unlike ambient air, the soil possesses high thermal mass, creating a dampened response to external temperature fluctuations. The model calculates the effective ground temperature using an Exponential Moving Average (EMA) to simulate this inertia:

$$T_{ground,t} = (\alpha_{soli} \cdot T_{air,t}) + (1 - \alpha_{soli}) \cdot T_{ground,t-1} \quad (16)$$

Where:

- α_{soli}: The thermal coupling coefficient (set to 0.05). This low value ensures that only 5% of the current air temperature affects the soil, reflecting the significant time lag and "thermal memory" of the earth at burial depth.

The weakest points in an underground circuit are the cable joints. These components exhibit higher thermal gradients due to the use of insulating resins which have lower thermal conductivity than the cable insulation itself.
The model applies a fixed penalty to account for the restricted dissipation in joint housings:

$$T_{joint} = T_{op} + (L^2 \cdot 6.5) \quad (17)$$

This +6.5°C rise at full load represents the concentrated thermal stress that accelerates the chemical degradation of the joint's dielectric strength.

While cables are shielded, joints are susceptible to moisture infiltration over time, especially in saturated soils. The model triggers a power-law penalty when humidity (H) exceeds 85%:

$$\pi_{hum\_joint} = \begin{cases} (H/100)^4 & if\ H > 85 \\ 1.0 & otherwise \end{cases} \quad (18)$$

The local failure rate for the joint is calculated using an Arrhenius-style reliability model, combining thermal aging and moisture-induced dielectric breakdown:

 doi:10.20944/preprints202603.2315.v1

$$\lambda_{joint} = (1.5 \text{ x } 10^{-6}) \cdot e^{0.055 \cdot T_{joint}} \cdot \pi_{hum\_joint} \quad (19)$$

- **Thermal Aging:** The exponential term $e^{0.055 \cdot T_{joint}}$ reflects the "10-degree rule," where every significant increase in operating temperature drastically reduces the expected life of the insulation.
- 1.5 x 10^{-6}: represents the baseline failure rate, accounting for the joint's inherent reliability under nominal operating conditions

In addition to thermal and dielectric degradation, underground systems are vulnerable to the physical behavior of the surrounding earth. The model tracks a specific penalty for mechanical stress induced by extreme dry spells.

2.3.4. PV Systems: Clogging and Humidity-Induced Aging

Reliability Model for Power Electronics

The model addresses the degradation of Inverters by integrating thermal, environmental, and electrical stressors.
The internal operating temperature (T_{op}) is calculated by superimposed ambient temperature (T_{amb}) and a load-dependent thermal rise (T_{rise}). The thermal rise incorporates both Joule losses and switching losses, adjusted by cooling efficiency and maintenance-related degradation:

$$T_{rise} = (0.05 \cdot L + 0.05 \cdot L^2) \cdot 30.0 \cdot \eta_{cool} \cdot \text{CF} \quad (20)$$

Where:

- L: The per-unit loading profile.
- CF (Clogging Factor): Accounts for the linear accumulation of debris on heat sinks over time (t_{total}): CF=1.0+(t_{total}/150000.0).
- η_{cool} (Cooling Efficiency): Represents the loss of heat dissipation capacity above 35∘C:

$$\eta_{cool} = 1.0 + \left(\frac{\max(0, t_{amb} - 35.0)}{15.0}\right) \cdot 0.5 \quad (21)$$

The final operational temperature is capped at to simulate hardware thermal protection:

$$T_{op} = min(T_{amb} + T_{rise}, 95.0) \quad (22)$$

To model the degradation of solder joints due to thermal cycling, the Norris-Landzberg adaptation of the Coffin-Manson relation is employed. This factor π_{si} (Eq. 5) accounts for the frequency of cycles, the temperature swing, and the peak temperature.
In this formulation, m = 2.2 represents the fatigue exponent for lead-free solder and $\Delta T_{cycling}$ is the operational temperature swing.

The model integrates external climatic stressors into a composite factor ($\pi_{extreme} = \pi_{heat} + \pi_{hum}$). For power electronics, the primary drivers are extreme heat and high humidity:

- Extreme Heat: If $T_{max} > 40°C$, the impact is modeled quadratically: $\pi_{heat}=0.5 \cdot (T_{max}/40.0)^2$.

 doi:10.20944/preprints202603.2315.v1

- Humidity: If RH > 90%, a discrete penalty π_{hum}=0.3 is applied to account for corrosion and leakage currents.

Furthermore, Voltage Stress (π_v) is modeled using the Inverse Power Law to account for dielectric degradation when the operating voltage (V_{pu}) exceeds nominal levels:

$$\pi_v = \begin{cases} (V_{pu}/1.0)^4 & if\ V_{pu} > 1.02 \\ 1.0 & otherwise \end{cases} \quad (23)$$

PV Module Degradation and Thermal Modeling

The reliability model for PV modules focuses on the synergistic effects of solar irradiance, thermal cycling, and environmental stressors. Unlike active electronic components, the PV module's stress is primarily driven by external meteorological forcing rather than internal electrical loading.
The model estimates the cell's operating temperature (Top) by considering the instantaneous energy balance between ambient temperature and solar-induced heating. The relationship is governed by:

$$T_{op} = T_{amb} + (G_{solar} \cdot 0.025) \quad (24)$$

Where:

- G_{solar} (W/m^2): The incident solar irradiance.
- 0.025 (°C· m^2/W): The Ross Coefficient (thermal sensitivity factor). This coefficient represents the increase in cell temperature per unit of solar radiation, accounting for the module's thermal resistance and heat dissipation efficiency.

The average annual cell temperature (T_{cell_avg}) is then computed as the arithmetic mean of the resulting vector to characterize the continuous steady-state aging process.
PV modules are subject to significant mechanical stress due to the mismatch in the Coefficients of Thermal Expansion (CTE) between the silicon cells, the glass front, and the polymer backsheet. This degradation is modeled using the Norris-Landzberg equation adapted for PV fatigue (Eq. 5) [21].
For PV modules, the model assumes a Fatigue Exponent m = 2.2, which correlates with the degradation of inter-cell ribbon interconnects and solder bonds. The temperature delta ($\Delta T_{cycling}$) is defined by the daily and seasonal fluctuations between the peak cell temperature (T_{max}) and the nightly minimum.

2.3.5. BESS: Electro-Thermal Stress and Internal Cell Kinetics

The BESS reliability model is designed to capture the degradation of Li-ion chemistries, which is highly sensitive to the internal thermal state of the cells. The failure rate $\lambda_{BESS}$is defined as:

$$\lambda_{BESS} = \lambda_{base} \cdot \pi_{tech} \cdot \pi_{thermal,BESS} \cdot \left(1 + \pi_{ext_{temp}}\right) \quad (24)$$

The core of this model lies in the calculation of the internal cell temperature (T_{batt}) and its subsequent impact on the thermal acceleration factor:

- Internal Heating Estimation (T_{batt}): The cell temperature is not static but fluctuates based on the C-rate (current throughput). It is estimated through a non-linear Joule heating model:

 doi:10.20944/preprints202603.2315.v1

$$T_{batt} = T_{amb} + k_{batt} \cdot | I_{load} |^{1.8} \quad (25)$$

where $| I_{load} |$ is the hourly normalized current (p.u.), k_{batt} (40 K/p.u.) represents the thermal resistance of the battery pack, and the exponent 1.8 accounts for the non-linear relationship between current density and heat generation [12].

Thermal Acceleration Factor ($\pi_{thermal,BESS}$): The calculated T_{batt} is then used as the operational temperature (T_{op}) in the Arrhenius-based fatigue model:

$$\pi_{thermal,BESS} = \left(\frac{T_{batt} - T_{amb}}{T_{ref\_range}}\right)^{m} \cdot exp\left[\frac{E_a}{k_B}\left(\frac{1}{T_{ref}} - \frac{1}{T_{batt}}\right)\right] \quad (26)$$

This link ensures that high-power charge/discharge cycles directly accelerate the failure rate by increasing the exponential term of the equation.

External Stress Penalty (π_{ext_temp}): To account for the saturation of the active cooling system and Battery Management System (BMS) stress, a step-penalty $\pi_{ext\_temp} = 0.8$ is triggered whenever the ambient temperature T_{amb} exceeds 40°C. This represents the increased risk of thermal runaway or protective shutdowns under extreme climate conditions.

2.3.6. Switchgear and Monitoring Units (RTUs): Mechanical Wear and Environmental Corrosion

Unlike power transformers or conductors, the reliability of protective devices (circuit breakers, reclosers) and Remote Terminal Units (RTUs) is predominantly governed by the cumulative mechanical fatigue of moving parts and the chemical degradation of control electronics. The instantaneous failure rate λ_{SW} is formulated as:

$$\lambda_{SW} = \lambda_{base} \cdot \pi_{tech} \cdot \pi_{mech} \cdot (1 + \pi_{corr}) \quad (27)$$

The model explicitly accounts for two primary stress-driven degradation pathways:

- Mechanical Fatigue of Actuation Systems (π_{mech}): The reliability of switching devices is strongly correlated with the number of duty cycles performed. Each operation induces mechanical stress on springs, latches, and contact surfaces. This is modeled using a power-law relationship based on the cumulative number of operations (N_{ops}):

$$\pi_{mech} = \left(\frac{N_{ops}}{1000}\right)^{1.5} \quad (28)$$

where the exponent 1.5 represents the accelerated wear-out phase as the device approaches its mechanical endurance limit. This factor ensures that highly active assets (e.g., those managing frequent reconfigurations or PV-driven fluctuations) exhibit higher failure probabilities than idle ones.

- Atmospheric Corrosion and Dielectric Breakdown (π_{corr}): RTUs and switchgear enclosures are sensitive to high humidity, which promotes the oxidation of metallic contacts and the formation of conductive paths on Printed Circuit Boards (PCBs) through dendritic growth. To capture this, an environmental penalty is introduced:

$$\pi_{corr} = \begin{cases} 0.20 & \text{if } H_{rel} > 85\% \\ 0.00 & \text{otherwise} \end{cases} \quad (29)$$

A constant multiplier of 0.2 is triggered when the relative humidity (H_{rel}) exceeds 85%, representing a 20% increase in the failure rate due to moisture-induced degradation of the control circuitry and insulation integrity [17].

 doi:10.20944/preprints202603.2315.v1

By integrating these factors, the framework captures the "hidden" reliability cost of high-frequency network switching and the vulnerability of distributed automation hardware to local microclimates.

3. Case study and simulation tests

The reliability model was validated using a medium-voltage (MV) rural distribution network, specifically the ATL_Rete_Rurale_cluster_AM_BAU_2030 model. This grid is part of the digital archive developed by the ATLANTIDE project (Telematic Archive for the National Reference of Electrical Distribution Network).

The selected test system represents a "Business As Usual" (BAU) evolution scenario projected for the year 2030. It features a radial architecture comprising 83 buses and 81 lines, with a single power transformer at the primary substation serving as the Slack bus.

Aligned with the ATLANTIDE goal of modeling high-penetration renewable scenarios, the network includes 19 Photovoltaic (PV) units. A defining characteristic of this cluster is its 100% reliance on overhead lines, reflecting the typical infrastructure of the Italian rural landscape. To evaluate the impact of the climate stressors, the average annual MTBF (aggregated across all grid components) was benchmarked. Specifically, a "Base Scenario" (constant 25°C and no environmental forcing), was compared against a "Stressed Scenario" modeled on the RCP8.5 pathway, revealing the degradation in reliability under a 'business-as-usual" climate future.

Specifically, the RCP8.5 (Representative Concentration Pathway 8.5) represents the "worst-case" or "Business-as-Usual" trajectory defined by the IPCC (Intergovernmental Panel on Climate Change). It assumes a future where greenhouse gas emissions continue to rise significantly throughout the 21st century, leading to a radiative forcing of 8.5 W/m2 by 2100.

The impact of various climatic stressors per component was evaluated and it is presented in Table 3. For each asset, the table highlights the dominant stressor, the resulting MTBF (with and without the stressor), and the relative percentage decrease in reliability (impact of climatic stressors).

Table 3. "Identikit" of the network's health.

Component	Type	Age [y]	MTBF Base[y]	MTBF in presence of climatic stressors[y]	Impact of climatic stressors [%]	Dominante failure cause
PV_Inv_9	Converter	11.0	8.05	2.75	65.9	Heat Wave
PV_Inv_0	Converter	10.0	8.27	2.82	65.8	Heat Wave
PV_Inv_17	Converter	10.0	8.27	2.82	65.8	Heat Wave
PV_Inv_2	Converter	9.0	8.51	2.91	65.8	Heat Wave
PV_Inv_4	Converter	9.0	8.51	2.91	65.8	Heat Wave
PV_Inv_1	Converter	9.0	8.51	2.91	65.8	Heat Wave
PV_Inv_14	Converter	9.0	8.51	2.91	65.8	Heat Wave
PV_Inv_8	Converter	9.0	8.51	2.91	65.8	Heat Wave
PV_Inv_16	Converter	8.0	8.78	3.01	65.8	Heat Wave
PV_Inv_12	Converter	8.0	8.78	3.01	65.8	Heat Wave
PV_Inv_7	Converter	7.0	9.09	3.12	65.7	Heat Wave
PV_Inv_15	Converter	7.0	9.09	3.12	65.7	Heat Wave
PV_Inv_13	Converter	6.0	9.47	3.25	65.7	Heat Wave
PV_Inv_5	Converter	6.0	9.47	3.25	65.7	Heat Wave
PV_Inv_6	Converter	5.0	9.91	3.41	65.6	Heat Wave
PV_Inv_3	Converter	4.0	10.47	3.60	65.6	Heat Wave
PV_Inv_11	Converter	4.0	10.47	3.60	65.6	Heat Wave
PV_Inv_18	Converter	3.0	11.20	3.85	65.6	Heat Wave

 doi:10.20944/preprints202603.2315.v1

PV_Inv_10	Converter	3.0	11.20	3.86	65.6	Heat Wave
RTU_0	RTU	3.0	11.20	3.87	65.4	Heat Wave
Line_9	Overhead Line	50.0	65.36	10.18	84.4	Wind/Weather
Line_37	Overhead Line	50	65.36	10.18	84.4	Wind/Weather
PV_Mod_3	PV_Module	11	32.21	10.37	84.4	Aging/Thermal
Line_24	Overhead Line	49	66.67	10.38	67.8	Wind/Weather
Line_52	Overhead Line	49	66.67	10.38	84.4	Wind/Weather
Line_19	Overhead Line	49	66.67	10.38	84.4	Wind/Weather
Line_56	Overhead Line	48	68.03	10.59	84.4	Wind/Weather
Line_51	Overhead Line	47	69.45	10.82	84.4	Wind/Weather
PV_Mod_4	Overhead Line	10	33.64	10.86	67.7	Aging/Thermal
Line_79	Overhead Line	46	70.93	11.05	84.4	Wind/Weather
Line_36	Overhead Line	45	72.47	11.29	84.4	Wind/Weather
Line_3	Overhead Line	45	72.47	11.29	84.4	Wind/Weather
Line_4	Overhead Line	44.0	74.08	11.54	84.4	Wind/Weather
Line_44	Overhead Line	43.0	75.56	11.80	84.4	Wind/Weather
Line_23	Overhead Line	41.0	79.37	12.36	84.4	Wind/Weather
Line_55	Overhead Line	41.0	79.37	12.36	84.4	Wind/Weather
Line_32	Overhead Line	40.0	81.30	12.66	84.4	Wind/Weather
PV_Mod_5	PV_Module	7.0	39.44	12.84	67.5	Aging/Thermal
PV_Mod_8	PV_Module	7.0	39.44	12.84	67.5	Aging/Thermal
PV_Mod_12	PV_Module	7.0	39.44	12.84	67.5	Aging/Thermal
Line_80	Overhead Line	39.0	83.34	12.98	84.4	Wind/Weather
Line_64	Overhead Line	39.0	83.34	12.98	84.4	Wind/Weather
Line_42	Overhead Line	38.0	85.47	13.31	84.4	Wind/Weather
Line_70	Overhead Line	37.0	87.72	13.66	84.4	Wind/Weather
Line_8	Overhead Line	37.0	87.72	13.66	84.4	Wind/Weather
Line_22	Overhead Line	36.0	90.09	14.03	84.4	Wind/Weather

 doi:10.20944/preprints202603.2315.v1

Line_10	Overhead Line	36.0	90.09	14.03	84.4	Wind/Weather
Line_34	Overhead Line	35.0	92.60	14.42	84.4	Wind/Weather
Line_75	Overhead Line	35.0	92.60	14.42	84.4	Wind/Weather
Line_66	Overhead Line	34.0	95.24	14.83	84.4	Wind/Weather
Line_17	Overhead Line	34.0	95.24	14.83	84.4	Wind/Weather
Line_80	Overhead Line	39.0	83.34	12.98	84.4	Wind/Weather
PV_Mod_9	PV_Module	5.0	45.55	14.90	67.3	Aging/Thermal
PV_Mod_18	PV_Module	5.0	45.55	14.90	67.3	Aging/Thermal
Line_0	Overhead Line	31.0	104.7	16.22	84.4	Wind/Weather
Line_40	Overhead Line	31.0	104.7	16.22	84.4	Wind/Weather
Line_54	Overhead Line	31.0	104.7	16.22	84.4	Wind/Weather
Line_45	Overhead Line	31.0	104.7	16.22	84.4	Wind/Weather
Line_65	Overhead Line	31.0	104.7	16.22	84.4	Wind/Weather
Line_2	Overhead Line	30.0	107.53	16.75	84.4	Wind/Weather
Line_15	Overhead Line	30.0	107.53	16.75	84.4	Wind/Weather
Line_25	Overhead Line	30.0	107.53	16.75	84.4	Wind/Weather
Line_62	Overhead Line	30.0	107.53	16.75	84.4	Wind/Weather
Line_53	Overhead Line	30.0	107.53	16.75	84.4	Wind/Weather
Line_28	Overhead Line	30.0	107.53	16.75	84.4	Wind/Weather
Line_21	Overhead Line	30.0	107.53	16.75	84.4	Wind/Weather
Line_31	Overhead Line	30.0	107.53	16.75	84.4	Wind/Weather
Line_7	Overhead Line	30.0	107.53	16.75	84.4	Wind/Weather
Line_5	Overhead Line	30.0	107.53	16.75	84.4	Wind/Weather
Line_35	Overhead Line	30.0	107.53	16.75	84.4	Wind/Weather
Line_33	Overhead Line	30.0	107.53	16.75	84.4	Wind/Weather
Line_59	Overhead Line	30.0	107.53	16.75	84.4	Wind/Weather
Line_59	Overhead Line	30.0	107.53	16.75	84.4	Wind/Weather

 doi:10.20944/preprints202603.2315.v1

Line_27	Overhead Line	27.0	119.05	18.54	84.4	Wind/Weather
Line_77	Overhead Line	27.0	119.05	18.54	84.4	Wind/Weather
Line_1	Overhead Line	27.0	119.05	18.54	84.4	Wind/Weather
Line_78	Overhead Line	27.0	119.05	18.54	84.4	Wind/Weather
Line_13	Overhead Line	27.0	119.05	18.54	84.4	Wind/Weather
Line_48	Overhead Line	27.0	119.05	18.54	84.4	Wind/Weather
Line_68	Overhead Line	27.0	119.05	18.54	84.4	Wind/Weather
Line_38	Overhead Line	27.0	119.05	18.54	84.4	Wind/Weather
Line_50	Overhead Line	27.0	119.05	18.54	84.4	Wind/Weather
Line_12	Overhead Line	30.0	107.53	16.75	84.4	Wind/Weather
Line_69	Overhead Line	27.0	119.05	18.54	84.4	Wind/Weather
Line_20	Overhead Line	30.0	107.53	16.75	84.4	Wind/Weather
Line_41	Overhead Line	27.0	119.05	18.54	84.4	Wind/Weather
Line_6	Overhead Line	30.0	107.53	16.75	84.4	Wind/Weather
Line_58	Overhead Line	22.0	144.93	22.57	84.4	Wind/Weather
Line_73	Overhead Line	22.0	144.93	22.57	84.4	Wind/Weather
Line_60	Overhead Line	22.0	144.93	22.57	84.4	Wind/Weather
Line_46	Overhead Line	22.0	144.93	22.57	84.4	Wind/Weather
Line_14	Overhead Line	22.0	144.93	22.57	84.4	Wind/Weather
Line_30	Overhead Line	22.0	144.93	22.57	84.4	Wind/Weather
Line_57	Overhead Line	22.0	144.93	22.57	84.4	Wind/Weather
Line_26	Overhead Line	22.0	144.93	22.57	84.4	Wind/Weather
Line_18	Overhead Line	22.0	144.93	22.57	84.4	Wind/Weather
Line_16	Overhead Line	22.0	144.93	22.57	84.4	Wind/Weather
Line_29	Overhead Line	22.0	144.93	22.57	84.4	Wind/Weather
Line_39	Overhead Line	22.0	144.93	22.57	84.4	Wind/Weather

 doi:10.20944/preprints202603.2315.v1

Line_49	Overhead Line	22.0	144.93	22.57	84.4	Wind/Weather
Line_63	Overhead Line	22.0	144.93	22.57	84.4	Wind/Weather
Line_11	Overhead Line	22.0	144.93	22.57	84.4	Wind/Weather
Line_76	Overhead Line	22.0	144.93	22.57	84.4	Wind/Weather
Line_61	Overhead Line	22.0	144.93	22.57	84.4	Wind/Weather
Line_43	Overhead Line	22.0	144.93	22.57	84.4	Wind/Weather
Line_47	Overhead Line	22.0	144.93	22.57	84.4	Wind/Weather
Line_74	Overhead Line	22.0	144.93	22.57	84.4	Wind/Weather
Line_71	Overhead Line	22.0	144.93	22.57	84.4	Wind/Weather
Line_72	Overhead Line	22.0	144.93	22.57	84.4	Wind/Weather
Line_67	Overhead Line	22.0	144.93	22.57	84.4	Wind/Weather
Trafo_0	Transformer	40.0	107.20	69.27	35.4	Aging/Thermal

Figures 2 and 3 present screenshots captured from the tool's dashboard. In detail, Figure 2 displays the reliability status of the individual grid components, while Figure 3 illustrates the simulated climatic conditions, including the maximum, mean, and minimum monthly values for temperature, solar irradiance, wind speed, and humidity.

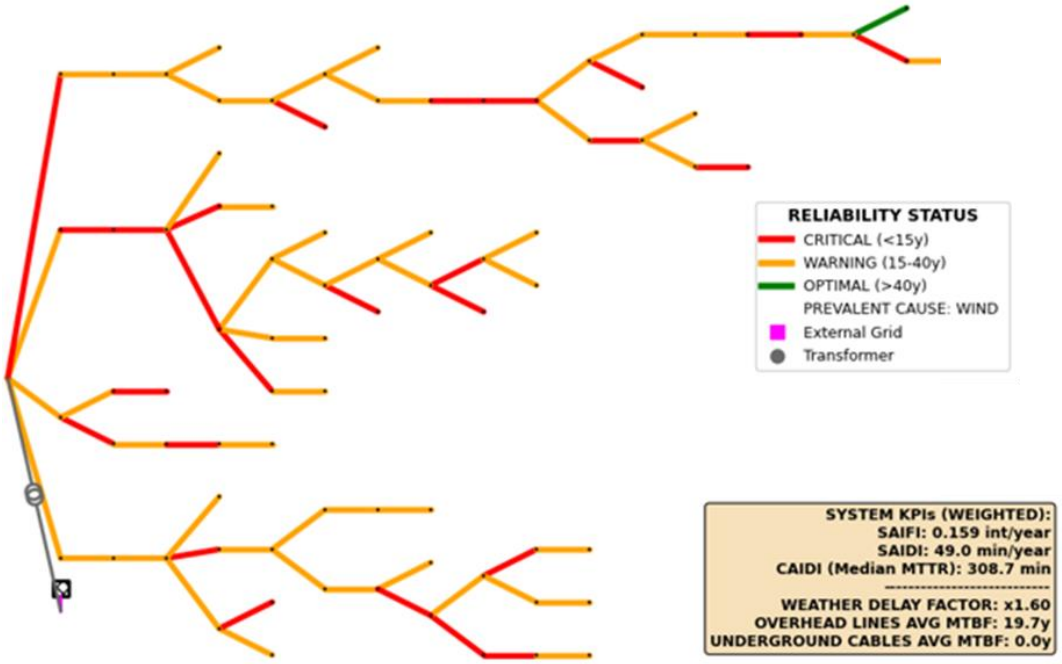

Figure 1. Network Health Mapping.

 doi:10.20944/preprints202603.2315.v1

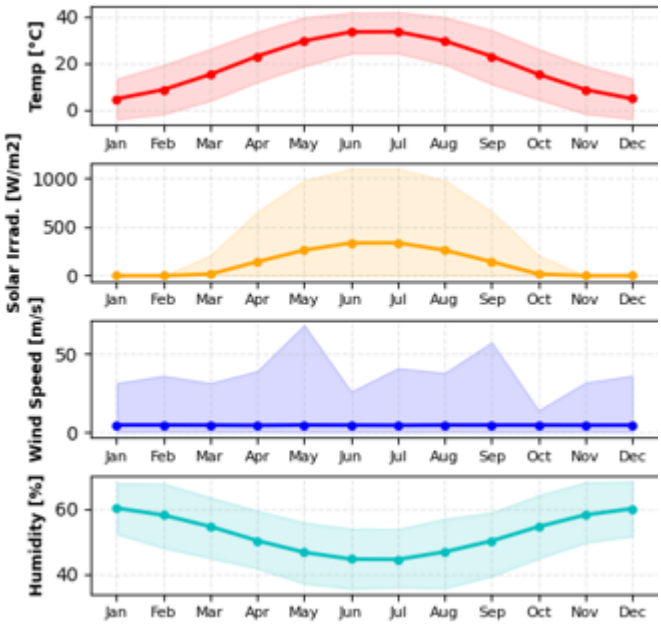

Figure 2. Climatic scenario.

4. Results and discussion

Our findings highlighted a rapid degradation process driven by the synergistic coupling of thermal and operational stressors. As detailed in Table 3, overhead lines experienced a reliability drop exceeding 80%, while PV inverters recorded a 65% reduction. Despite the higher percentage loss in passive assets, the decline in inverters is arguably more critical given their architectural complexity and systemic importance. For an inverter at its mid-life stage, the MTBF was slashed from 8.05 to 2.75 years. This sharp contraction emphasizes the extreme sensitivity of power electronics to climate-driven forcing, particularly under high-emission trajectories like the RCP8.5 scenario. Consequently, this study underscores the imperative need to transition from static reliability benchmarks to dynamic frameworks that incorporate environmental variables.

Furthermore, the analysis confirmed a robust correlation between asset seniority and failure probability, revealing a distinct divergence in how different technologies respond to climate pressure:

- PV Modules: Older units (e.g., 27 years) exhibited a failure mode dominated by accelerated thermo-mechanical aging, leading to a 67% MTBF reduction.
- Overhead Lines: These assets represented a spatially distributed vulnerability; for segments with over 50 years of service, wind-induced mechanical stress emerged as the primary failure driver, pushing reliability levels significantly below standard industry expectations.
- Power Transformers: In contrast, the main transformer (Trafo_0) demonstrated remarkable resilience, maintaining an MTBF of 69.27 years despite its 40-year service history. While it remains a high-stakes node for grid security, its physical characteristics provide superior buffering against the environmental forcing that cripples power electronics.

The simulation, executed at a network-wide scale, successfully integrated temporal reliability (MTBF) with economic risk (OPEX). For the ATL_Grid_Rural cluster, the framework identified a total projected OPEX risk of €39,875.85 for the study year. Given the grid's reliance on 19 PV units and 81 overhead lines, these results demonstrate how technical degradation translates directly into quantifiable financial exposure.

Ultimately, these outcomes validate the core hypothesis: traditional, static reliability models—such as those derived from MIL-HDBK-217—tend to significantly overestimate asset longevity by neglecting the nonlinear coupling the synergistic effects of operational loads and environmental forcing. Our data regarding RTUs and inverters, which show MTBFs falling below the 10-year threshold, align with recent field evidence identifying humidity-driven corrosion and thermal fatigue

 doi:10.20944/preprints202603.2315.v1

as the "silent killers" of grid digitalization. By leveraging the Norris-Landzberg model, this framework bridges the gap between theoretical power flow and practical asset management. While electronics exhibit higher failure frequencies, the economic weight of transformers remains disproportionately high due to replacement costs and energy-not-served penalties. This necessitates a shift toward site-specific, climate-resilient maintenance strategies to ensure long-term grid stability.

5. Conclusions

The proposed framework establishes a multi-physics approach for the dynamic reliability assessment of modern distribution grids by shifting the analytical paradigm from static, age-based failure models to an environmental-aware Physics-of-Failure (PoF) methodology. This research effectively captures the complex interplay between electrical loading and microclimatic stressors, demonstrating that the integration of an advanced analytical dashboard represents a significant step forward in grid risk management. By providing DSOs with a dual-layer perspective, the tool allows for the quantification of system-wide resilience through macro-level KPIs such as SAIFI, SAIDI, and the Weather Delay Factor, while simultaneously enabling prioritized, condition-based maintenance via micro-level asset-specific MTBF rankings.

A fundamental insight emerging from this work is the critical role of auxiliary components, such as RTUs, which are frequently omitted in standard benchmarks like the CIGRE MV network. Integrating these components into the simulation highlights them as critical reliability bottlenecks, particularly susceptible to humidity-induced degradation. This enables DSOs to conduct advanced 'What-If' scenarios to quantify the ERC associated with grid digitalization prior to its physical implementation. The empirical evidence obtained from the rural distribution cluster confirms that environmental forcing can reduce the MTBF by over 80% compared to baseline models, with critical active components such as inverters experiencing a lifespan contraction to approximately 2.7 years during extreme heatwaves. The calculated annual OPEX risk of €39,875.85 further underscores that the operational life of grid infrastructure is a dynamic function of environmental exposure rather than a fixed chronological value. While the current framework provides a robust estimation tool, future research will address existing limitations by incorporating stochastic Mean Time To Repair (MTTR) models to account for weather-related logistical delays and exploring the dynamics of "Reliability Contagion," where localized failures, such as cooling system clogs, trigger cascading thermal effects. Additionally, the implementation of machine learning to refine the Clogging Constant based on real-time sensor data is expected to further enhance the framework's predictive accuracy. Ultimately, by transitioning the maintenance strategy from chronological age to physical-exposure-based risk, this methodology offers a robust decision-support system for the cost-effective hardening of Smart Grids against the increasing threats of climate-driven stressors.

Author Contributions: Conceptualization: R.C.; methodology: R.C.; model implementation: R.C. a; data curation: R.C., M.V.; writing—review and editing: R.C., M.V. All authors have read and agreed to the published version of the manuscript.

Funding: This work has been funded by the Research Fund for the Italian Electrical through the project "Accordo di Programma 2025–2027—Project 2.3a" between ENEA and the Ministry of the Environment and Energetic Safety (MASE).

Data Availability Statement: The data presented in this study are available on request from the corresponding author.

Conflicts of Interest: The authors declare no conflict of interest.

References

1. Kesphrom, N., Nedphokaew, S., Ruangsap, N., & Rugthaicharoencheep, N. (2025). Power Distribution System Improvement Planning Considering Financial Losses Due to Faults in Power Systems. Energies, 18(4), 938. https://doi.org/10.3390/en18040938. Available at: https://www.mdpi.com/1996-1073/18/4/938

 doi:10.20944/preprints202603.2315.v1

2. Zhang, X., et al. (2023). Reliability Evaluation of Distribution System Based on Time Varying Failure Rates. IEEE (Open Access). Available at: https://ieeexplore.ieee.org/document/10257125
3. Parol, M., Wasilewski, J., Wojtowicz, T., Arendarski, B., & Komarnicki, P. (2022). Reliability Analysis of MV Electric Distribution Networks Including Distributed Generation and ICT Infrastructure. Energies, 15(15), 5311. https://doi.org/10.3390/en15145311 Available at: https://www.researchgate.net/publication/362176550_Reliability_Analysis_of_MV_Electric_Distribution_Networks_Including_Distributed_Generation_and_ICT_Infrastructure/fulltext/62e1667d4246456b55eec6d9/Reliability-Analysis-of-MV-Electric-Distribution-Networks-Including-Distributed-Generation-and-ICT-Infrastructure.pdf
4. Karngala, A. K., Singh, C., & Xie, L. (2023). Predictive Reliability Assessment of Distribution Grids with Residential Distributed Energy Resources. Available at: https://arxiv.org/pdf/2312.06154
5. Téllez, A. A., Krishnan, N., García, E., Carrión, D., & Ruiz, M. (2025). A Probabilistic Framework for Reliability Assessment of Active Distribution Networks with High Renewable Penetration Under Extreme Weather Conditions. Energies, 18(24), 6525. https://doi.org/10.3390/en18246525. Available at: https://www.mdpi.com/1996-1073/18/24/6525.
6. Rouholamini, M., Wang, C., Magableh, S., & Wang, X. (2025). Resiliency of electric power distribution networks: A review. Journal of Infrastructure Preservation and Resilience, 6, 39. https://doi.org/10.1186/s43065-025-00154-y. Available at: https://link.springer.com/article/10.1186/s43065-025-00154-y#citeas.
7. Gonçalves, A. C. R., Costoya, X., Nieto, R., & Liberato, M. L. R. (2024). Extreme weather events on energy systems: a comprehensive review on impacts, mitigation, and adaptation measures. Sustainable Energy Research, 11, 4. DOI: https://doi.org/10.1186/s40807-023-00097-6. Available at: https://link.springer.com/article/10.1186/s40807-023-00097-6
8. Guddanti, K. P., Bharati, A. K., Nekkalapu, S., McWheter, J., & Morris, S. (2024). A Comprehensive Review: Impacts of Extreme Temperatures due to Climate Change on Power Grid Infrastructure and Operation. DOI: https://doi.org/10.48550/arXiv.2410.08425. Available at: https://arxiv.org/abs/2410.08425.
9. Kasimalla, S. R., Park, K., Zaboli, A., Hong, Y., & Hong, J. (2024). An Evaluation of Sustainable Power System Resilience in the Face of Severe Weather Conditions and Climate Changes: A Comprehensive Review of Current Advances. Sustainability, 16(7), 3047. DOI: https://doi.org/10.3390/su16073047. Available at: https://www.mdpi.com/2071-1050/16/7/3047.
10. Do, V., Wilner, L. B., Flores, N. M., McBrien, H., Northrop, A. J., & Casey, J. A. (2025). Spatiotemporal patterns of individual and multiple simultaneous severe weather events co-occurring with power outages in the United States, 2018–2020. PLOS Climate, 4(1), e0000523. DOI: https://doi.org/10.1371/journal.pclm.0000523. Available at: https://journals.plos.org/climate/article?id=10.1371/journal.pclm.0000523.
11. Adinolfi, G.; Ciavarella, R.; Graditi, G.; Ricca, A.; Valenti, M. A Planning Tool for Reliability Assessment of Overhead Distribution Lines in Hybrid AC/DC Grids. Sustainability 2021, 13, 6099. doi:10.3390/su13116099.
12. Adinolfi G., Ciavarella R., Graditi G., Ricca A., Valenti M. Innovative Method for Reliability Assessment of Power Systems: From Components Modeling to Key Indicators Evaluation, (2024) Electronics (Switzerland), 13 (2), art. no. 275, DOI: 10.3390/electronics13020275.
13. Ciavarella R., Graditi G., Valenti M., Strasser T.I., Innovative Frequency Controls for Intelligent Power Systems, (2018) SPEEDAM 2018 - Proceedings: International Symposium on Power Electronics, Electrical Drives, Automation and Motion, art. no. 8445275, pp. 656 - 660, DOI: 10.1109/SPEEDAM.2018.8445275.
14. CIGRE Working Group C6.11. *Development and Operation of Active Distribution Networks*; Technical Brochure 428; CIGRE: Paris, France, 2010.
15. R. He, H. Liang, J. Wu, H. Xie and M. Shahidehpour, Reliability Assessment of Cyber-Physical Distribution System Using Multi-Dimensional Information Network Model, in IEEE Transactions on Smart Grid, vol. 14, no. 6, pp. 4683-4692, Nov. 2023, doi: 10.1109/TSG.2023.3246955. Available at: https://ieeexplore.ieee.org/document/10049159.
16. Luo, F., Ge, N., Xu, J. (2023). Power Supply Reliability Analysis of Distribution Systems Considering Data Transmission Quality of Distribution Automation Terminals. Energies. Available at:

 doi:10.20944/preprints202603.2315.v1

https://www.researchgate.net/profile/Xiaohui-Ye/publication/311461367_Review_on_power_system_cascading_failure_thoeries_and_studies/links/5a7a678ea6fdccebdd819f73/Review-on-power-system-cascading-failure-thoeries-and-studies.pdf.

17. Weibull, W. A statistical distribution function of wide applicability. J. Appl. Mech. 1951, 18, 293–297.
18. Brown, R.E. Electric Power Distribution Reliability, 2nd ed.; CRC Press: Boca Raton, FL, USA, 2008.
19. Pecht, M.G. Prognostics and Health Management of Electronics; John Wiley & Sons: Hoboken, NJ, USA, 2008.
20. Wang, J.; Liu, P.; Hicks-Garner, J.; Sherman, E.; Soukiazian, S.; Verbrugge, M.; Tataria, H.; Musser, J.; Finamore, P. Cycle-life model for graphite-LiFePO4 cells under different discharge C-rates and temperatures. J. Power Sources 2011, 196, 3942–3948.
21. Norris, K.C.; Landzberg, A.H. Reliability of Hermetic Terminations on Steel-Clad Copper. IBM J. Res. Dev. 1969, 13, 266–271.